ADVANCED THERAPEUTICS
www.advtherap.com

In Vivo Combined Photoacoustic Imaging and Photothermal Treatment of HPV-Negative Head and Neck Carcinoma with NIR-Responsive Non-Persistent Plasmon Nano-Architectures

Valentina Frusca, Chiara Cavallini, Agata Zamborlin, Giuliana Drava, Virginia Barone, Lisa Gherardini, Mario Chiariello, Paolo Armanetti, Maria Laura Ermini, Luca Menichetti, and Valerio Voliani**

The combination of photoacoustic imaging (PAI) and photothermal therapy (PTT) is an attractive approach in cancer management due to the non-invasive features combined with real-time imaging and selective tissue damage by non-ionizing radiation. This approach is especially appealing for Head and Neck Squamous Cell Carcinoma (HNSCC) management, where up to 40% of patients require modifications of the treatment regimen. On the other hand, most of the agents developed for PAI/PTT suffer from persistence or re-shaping issues. Here, a unique non-persistent plasmon nano-architecture (*t*NAs-IRDye) is presented that simultaneously acts as a contrast agent for PAI and as a photothermal transducer for PTT. The *t*NAs-IRDye are fully characterized and evaluated in vitro and ex vivo, and their performance as theranostic agents is assessed in HPV-negative HNSCC murine models. A significant modulation of tumor growth is obtained in vivo upon intratumoral injection of *t*NAs-IRDye and subsequent NIR irradiation compared to the solely irradiated control. The outcomes of this study exhibit a noteworthy potential to foster the development of innovative clinical strategies for the management of HPV-negative head and neck carcinoma.

1. Introduction

Head and Neck Squamous Cell Carcinoma (HNSCC) ranks sixth in incidence worldwide.[1] HNSCCs arise from mucosal epithelial cells of the oral cavity, larynx, oropharynx, and hypopharynx undergoing first hyperplasia, then dysplasia, in situ carcinoma, and eventually invasive carcinoma.[2] Surgery and radiotherapy are usually employed in early-diagnosed cancers, whereas definitive cisplatin-based concurrent chemoradiotherapy (CRT) is required for the advanced stages usually involving regional lymph nodes (60% of diagnoses).[3] Up to 40% of patients require modifications of the treatment regimen (i.e., dose reduction, delays, and omissions) because of the adverse events associated with both platinum-based chemotherapy (such as renal insufficiency, electrolyte imbalances, myelo- and oto-toxicity)

V. Frusca, A. Zamborlin[+], M. L. Ermini, V. Voliani
Center for Nanotechnology Innovation@NEST
Istituto Italiano di Tecnologia
Piazza San Silvestro 12, Pisa 56127, Italy
E-mail: valerio.voliani@unige.it
V. Frusca
Scuola Superiore Sant'Anna
Piazza Martiri della Libertà 33, Pisa 56127, Italy

The ORCID identification number(s) for the author(s) of this article can be found under https://doi.org/10.1002/adtp.202400110

[+]Present address: Ghent Research Group on Nanomedicines, Department of Pharmaceutics, Ghent University, Ottergemsesteenweg 460, Ghent B-9000, Belgium

DOI: 10.1002/adtp.202400110

C. Cavallini, P. Armanetti, L. Menichetti
Institute of Clinical Physiology
Italian National Research Council
via Giuseppe Moruzzi 1, Pisa 56124, Italy
E-mail: luca.menichetti@ifc.cnr.it
A. Zamborlin[+]
NEST-Scuola Normale Superiore
Piazza San Silvestro 12, Pisa 56127, Italy
G. Drava, V. Voliani
Department of Pharmacy, School of Medical and Pharmaceutical Sciences
University of Genoa
Viale Cembrano 4, Genoa 16148, Italy
V. Barone
Department of Molecular and Developmental Medicine
University of Siena
Via Aldo Moro 2, Siena 53100, Italy
L. Gherardini, M. Chiariello
Institute of Clinical Physiology
Italian National Research Council and Core Research Laboratory (CRL)
Istituto per lo Studio
la Prevenzione e la Rete Oncologica (ISPRO)
Via Fiorentina 1, Siena 53100, Italy

and radiation-induced toxicity to the surrounding organs at risk.[4] Still, a significant proportion of patients will develop recurrent or metastatic disease that is no longer amenable to curative therapy and most of them succumb within a year of diagnosed recurrency and/or metastasis.[5] Thus, less toxic treatment strategies to improve the outcome of HNSCC patients are urgently required.[6]

In this regard, the combination of photoacoustic imaging (PAI) and photothermal therapy (PTT) has attracted attention due to its non-invasive characteristics, and the possibility of combining real-time imaging and selective tissue damage via non-ionizing radiation.[7–9] PAI is a promising technique that allows to obtain in vivo morphological, functional, and molecular characterization of neoplasms.[10] Exogenous contrast agents are generally used to improve the spatial resolution and the imaging depth limit of PAI in tissues and organs.[10,11] The most common agents are dyes or engineered plasmon nanoparticles.[12,13] The first ones usually demonstrate a fast clearance by the renal pathway but suffer from low specificity and poor photoacoustic (PA) signal, while the latter generally exhibit persistence issues.[12,14] In this regard, we developed hybrid nanomaterials (NAs-IRDye) that exploit the interactions between dyes and plasmonic ultrasmall gold nanoparticles (USNPs) to combine non-persistent building blocks with collectable near-infrared (NIR) PA signals in a single probe.[15,16] PTT exploits the effect induced by photothermal agents (PTAs), which efficiently convert NIR light into heat.[10] The consequent rise in the temperature may result in tumor ablation.[17] To date, several PTAs based on conducting polymers or plasmonic, semiconductor or carbon nanomaterials have been reported.[17,18] Among them, gold nanoparticles are of special appeal due to their intrinsic features, such as versatility and biocompatibility, with promising results for the treatment of oral squamous cell carcinoma.[19] Despite this encouraging context, no gold PTAs have yet obtained approval for clinical use either because of their excessive size (above the renal excretion threshold) or the reshaping of anisotropic geometries after PT transduction.[20,21] To overcome this limitation, few years ago we introduced the thermo-NAs (*t*NAs): NIR-responsive hybrid nanoplatforms showing efficient photothermal conversion without reshaping or loss of functionality even after multiple irradiation cycles.[21] The *t*NAs belong to the family of the ultrasmall-in-nano architectures (NAs), and are composed by a biodegradable silica capsule containing polymeric aggregates of USNPs.[22] The excretion profile of the building blocks of NAs has been comprehensively evaluated after intravenous and intranasal administration, and some potential applications in oncology for both the treatment of primary neoplasms and metastasis have been already demonstrated.[14,23–28]

Here, we introduce a unique nano-architecture (*t*NAs-IRDye) that conveniently combines the features of *t*NAs and NAs-IRDye. For the first time, the ability to act as a contrast agent for PAI and the capacity to perform as a photothermal agent for PTT are blended into a single platform. The *t*NAs-IRDye have been designed, fully characterized, and their performance in photoacoustic and photothermal application was evaluated in real-time diagnosis and treatment of HPV-negative head and neck murine models. This work confirms the potentiality of non-persistent *t*NAs-IRDye as photoacoustic/photothermal probes and may pave the way for the development of the next approaches for the management of head and neck carcinoma.

2. Results and Discussion

NAs are characterized by a modifiable silica capsule protecting the inner polymeric core embedding gold USNPs of ≈3 nm diameter.[22] The polymeric aggregates comprise two oppositely charged polymers that entrap the USNPs, namely poly(sodium 4-styrenesulfonate) (PSS, negatively charged), and poly(L-lysine) (PL, positively charged). The latter can be modified by covalent conjugation with dyes and/or prodrugs to expand the nanomedical potentiality.[16] NAs show an absorption maximum at 530 nm due to plasmon resonance.[23] The optical behavior of NAs can be modified by the addition of dimercaptostilbene (DMSB) to the reaction mixture, forming the *t*NAs. Indeed, DMSB reversibly aggregates Au USNPs causing a broadening of the primary plasmon peak with a red shift to 570 nm, and the development of a new small plasmon resonance at 810 nm.[21] The potential of *t*NAs as PTA has been fully investigated in cultured cells and 3D cancer models.[21,29] The novel nano-architecture (*t*NAs-IRDye) was produced by employing PL covalently modified with IRDye 800CW (**Figure 1**A), as in the standard protocol for NAs-IRDye production. The employment of PL-IRDye in the synthetic protocol does not affect the general geometry of the nano-architectures (Figure 1B). Indeed, the size and shell thickness were comparable among all the NAs (**Table 1**). The presence of IRDye in NAs and *t*NAs was confirmed by the new absorption band at 774 nm (Figure 1C), that was also employed to estimate the amount of IRDye per μg of gold (80 and 158 pmol μg^{-1} for NAs-IRDye and *t*NAs-IRDye, respectively).

The PA response of *t*NAs-IRDye and, as control, NAs-IRDye were characterized by means of a validated custom-made setup (Figure S1, Supporting Information) The results of PA analyses are summarized in Table S1 (Supporting Information). As expected, the PA multispectral trends (**Figure 2**; Figure S3, Supporting Information) for both the nano-architectures showed an absorption peak ≈800 nm and a good photostability. Interestingly, the signal intensity of *t*NAs-IRDye is 3x higher compared to NAs-IRDye at similar dye concentration, meaning that the *t*NAs-IRDye provide a more efficient heat conversion compared to NAs-IRDye. For both the nano-architectures, the analysis of the quality image parameters provided a Signal-To-Noise ratio (SNR) between 29 and 31, with a Contrast-to-Noise Ratio (CNR) between 28 and 29, and a coefficient of variation (CV) less than 3.5% (Table S1, Supporting Information).

The PA response of the nano-architectures was further assessed in a simulated in-vivo biological environment. The PA multispectral trends (Figure 2C,D) obtained from ex vivo samples of chicken breast injected with NAs-IRDye or *t*NAs-IRDye were found to be consistent with the signals analyzed in the previous characterization. Interestingly, the photostability tests showed an improvement in the image quality parameters in terms of CNR, SNR, and CV (Table S2, Supporting Information) for *t*NAs-IRDye. These results further confirmed that the combination of the nano-architectures with IRDye 800CW is a suitable strategy for photoacoustic imaging.[16]

To verify the suitability of *t*NAs-IRDye as photothermal agents, their photothermal performance was assessed in vitro

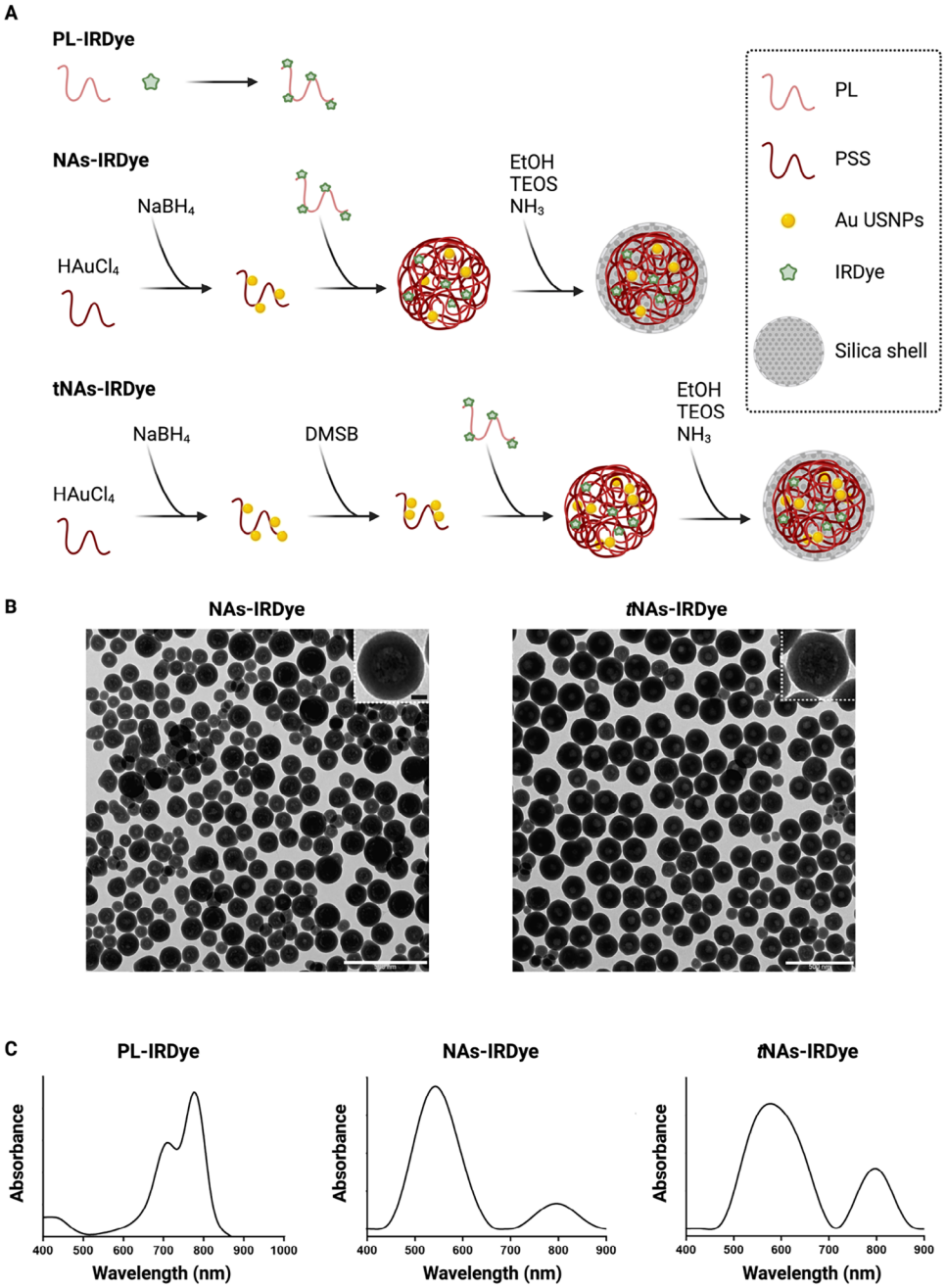

Figure 1. A) Schematic representation of the protocol for the synthesis of NAs-IRDye and *t*NAs-IRDye. After covalently conjugating IRDye 800CW to poly(L-lysine), the product was used to produce the arrays in both NAs-IRDye and *t*NAs-IRDye. The silica shell was produced following a modified Stöber protocol. B) TEM images of NAs-IRDye and *t*NAs-IRDye (scale bar: 500 nm). Inset: zoom on a nano-architecture (scale bar: 20 nm). C) UV–vis spectra of PL-IRDye, NAs-IRDye, and *t*NAs in PBS.

by recording the thermal profile of a solution of NAs-IRDye (as control) and *t*NAs-IRDye under continuous wave laser illumination (1000 s, 440 mW, Figure 2E). The rise of temperature in *t*NAs-IRDye and NAs-IRDye was reported in the graph, providing a clear comparison between the two platforms. The heating and cooling curves showed that both NAs-IRDye and *t*NAs-IRDye converted the absorbed photon energy into heat. However, as expected, *t*NAs-IRDye outperformed NAs-IRDye by increasing the temperature by 21 °C compared to the 12 °C rise of NAs-IRDye. Taken together, these data confirmed that *t*NAs-IRDye can be a suitable platform for combined PA/PTT.

To increase the complexity of the model, the potential of *t*NAs-IRDye was assessed in a murine xenograft model of HNSCCs. By considering both the in vitro and ex vivo data, two different *t*NAs-IRDye doses (2.5 and 5 μg of Au) were selected for intratumoral (IT) injection in tumor-bearing mice. Indeed, IT injection is a

Table 1. Comparison of the nano-architectures with or without IRDye.

	NAs	NAs-IRDye	*t*NAs	*t*NAs-IRDye
Diameter (TEM, nm)	98 ± 19	118.9 ± 22.1	124.3 ± 23.0	115.6 ± 32.2
Shell thickness (TEM, nm)	20.2 ± 1.6	20 ± 1.6	20.8 ± 2.3	20.5 ± 2.4
Hydrodynamic diameter in PBS (DLS, nm)	203.1 ± 1.9	233.4 ± 0.7	227.8 ± 4.0	221.9 ± 2.1
Zeta potential in PBS (mV)	−20.6 ± 0.4	−23.5 ± 2.1	−17.2 ± 1.1	−22.4 ± 2.4
Reference	[22]	[16]	[21, 29]	This manuscript

straightforward administration route for most HNSCCs to localize HT and avoid the nanomaterials' dispersion associated with systemic administration.[30,31] The laser power was optimized to obtain the best equilibrium between the thermal effect and potential damages to the illuminated skin.[32] Before the photothermal treatment, *t*NAs-IRDye distribution in the tumor volume (Figure S4 and Movie S1, Supporting Information) was detected through PAUS during the first 4 s, and the images were analyzed by a spectral unmixing tool (Movie S2, Supporting Information).

The PA signals acquired in the tumor before the injection of *t*NAs-IRDye (Day 0, **Figure 3A**) were exclusively derived from the endogenous oxy- and deoxy-haemoglobin (red and blue line, respectively). After injection (Day 0, Figure 3B), the PA signal of the nano-architectures (green line) was well detectable compared to the endogenous chromophores. On Day 1, the signal from *t*NAs-IRDye was confirmed in the tumor before PTT, and, after the treatment, PA spectral trend and spatial distribution of *t*NAs-IRDye were not affected by the CW laser illumination (Figure 3C; Figure S5, Supporting Information). The irradiation was performed for 10 min with an 808 nm CW laser leading to a mean power density of 0.67 W cm^{-2} in a selected spot size of 10 mm diameter. During the irradiation, the temperature of the tumor area was monitored by a NIR thermal camera. In the tumors injected with *t*NAs-IRDye, the temperature recorded on the top of the skin rapidly rose from a mean temperature of 31.1 to 40 °C. The temperature was then maintained at 40 °C with cycles of laser on/off to avoid damaging the surrounding healthy tissues. As expected, the thermal gradient during the first 100 s of laser illumination (Figure S6, Supporting Information) showed a dependency on the dose of *t*NAs-IRDye (ΔT of 5.2 and 3.3 °C for, respectively, 5 and 2.5 ug in gold of *t*NAs-IRDye). The means were significantly different with P-values respectively of 0.0485 and 0.1623 (One Way ANOVA, Matlab).

After PTT, the tumor volume was monitored by HF-US imaging (**Figure 4A**). The control tumors (only irradiation) rapidly and significantly increased in volume from day 0 to day 11, while tumors injected with *t*NAs-IRDye did not show significant growth over time (Figure 4B). Starting from day 2 after PTT, the volumes of the tumors treated with the nano-architectures were significantly smaller compared to the controls at each time point (p <0.001 for both doses on day 11 post-treatment), with slight differences between the two *t*NAs-IRDye doses only from day 11. Overall, the combined treatment resulted in an interesting modulation of tumor volume compared to the control, with a slightly better performance at higher dose.

Histological evaluation (Figure 4C) was performed on tumor excised from all the treated groups. A general tissue damage was observed in all the samples. NIR-treated tumor samples (Figure 4C, upper panels) showed the presence of several cells with normal appearance together with damaged cells showing cytoplasmic acidophilia, chromatin condensation, and enlarged cells with cytoplasmic vacuolization. The models treated with *t*NAs-IRDye (2.5 µg) + irradiation (Figure 4C, middle panels) displayed mostly damaged cells with cytoplasmic condensation and chromatin fragmentation, karyolysis, and cytosolic vacuolization, while the ones treated with *t*NAs-IRDye (5 µg) + irradiation (Figure 4C, lower panels) consisted of cells with almost complete nuclear destruction and enlarged vacuolated cytoplasm. In general, these data confirmed the increased efficiency of the photothermal treatment mediated by the nano-architectures.

3. Conclusion

Overall, we have added the first theranostic platform to the family of the non-persistent nano-architectures, showing both photoacoustic and photothermal features. The new tool has been fully characterized and evaluated, demonstrating that *t*NAs-IRDye are efficient contrast agents for real-time PAI and photothermal transducers for PTT. Even if the intratumoral injection may be recognized as a limitation of our study, it should be noted that it represents an ideal strategy that allows for the fine control of the injected amount of nano-architectures and it has been already used in several preclinical and clinical settings for the treatment of HNSCCs.[14,33,34] The nano-architectures were clearly identified in vivo in the carcinoma by exhibiting a consistent photoacoustic signal at the injection site for up to 24 h following the administration. They also demonstrated a promising PT effect in the NIR which led to a notable hyperthermic effect, resulting in a significant control of the tumor size. Taken together with the excretion trend of the building blocks and the ease of production, our findings suggest that *t*NAs-IRDye may provide a viable alternative for HPV-negative HNSCCs management by supporting real-time imaging and non-ionizing treatment.

4. Experimental Section

Synthesis of Poly(L-Lysine)-IRDye (PL-IRDye): Aqueous solution of poly(L-lysine) hydrobromide (75 µL of a 40 mg mL^{-1}) (PL, 15–30 kDa; Sigma-Aldrich, #7890) was mixed with 100 µL of acetate buffer 0.3 M pH 5.4 and with 2 µL of 8.57 mM solution of IRDye 800 CW NHS ester (Li-COR Biosciences GmbH, #929-70020) in dimethyl sulfoxide (DMSO). The mixture was incubated overnight under mild shaking at room temperature. The obtained conjugate poly(L-lysine)-IRDye (PL-IRDye) was used without further purification.

Synthesis of IRDye-Modified Nano-Architectures (NAs-IRDye): After adding 10 µL of poly(sodium 4-styrenesulfonate) (PSS, 70 kDa, 30% in

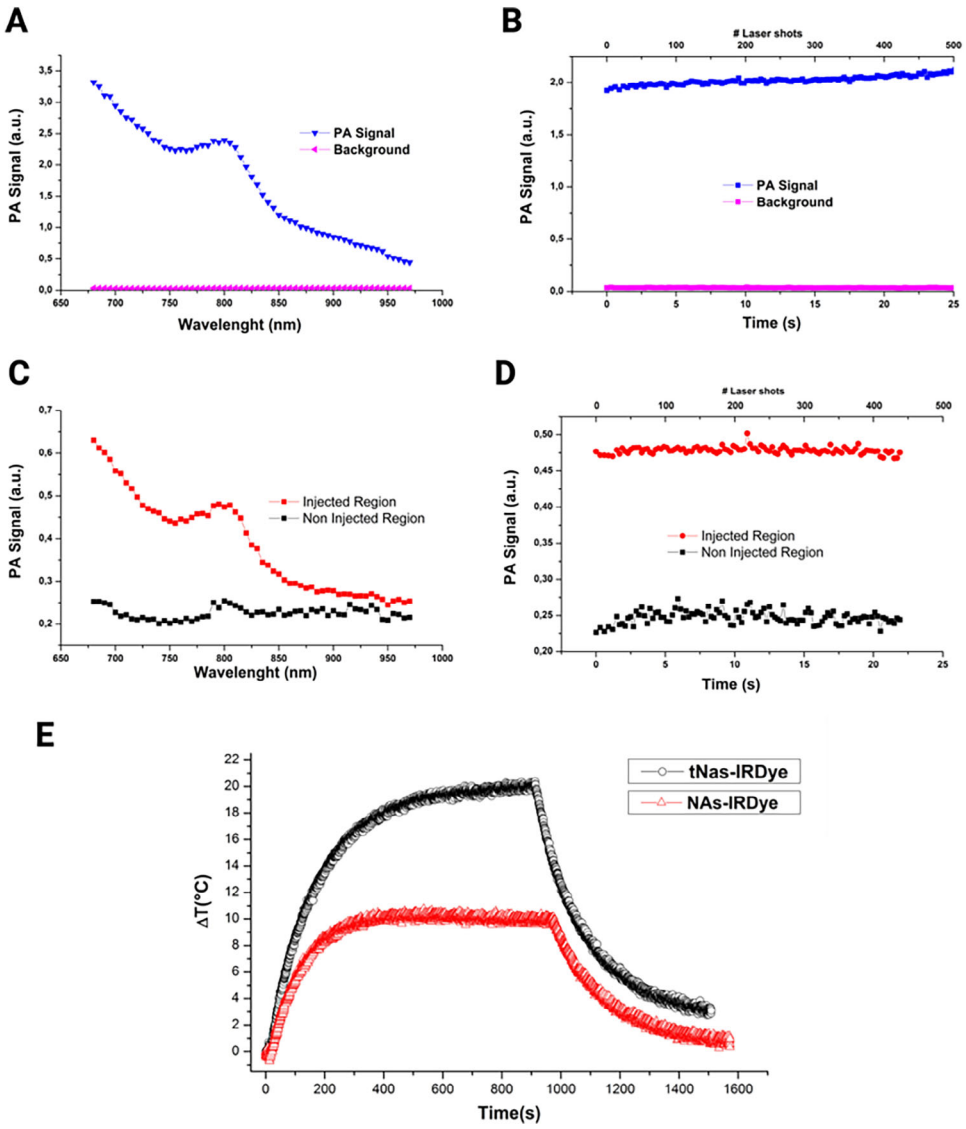

Figure 2. A) PA multispectral trend and B) photostability under prolonged 800 nm laser illumination of a solution of *t*NAs-IRDye at a concentration of 0.2 mg mL^{-1} in gold. C) PA multispectral trend and D) photostability of a 0.2 mg mL^{-1} bolus of *t*NAs-IRDye injected in an ex vivo sample of chicken breast (red dots: *t*NAs-IRDye, black dots: non-injected region). E) Thermal behavior of NAs-IRDye (red) and *t*NAs-IRDye (black) under CW laser illumination (440 mW, 808 nm, and 1000 s).

water; Sigma-Aldrich, #527 483) to 20 mL of Milli-Q water, the reduction of 200 µL of a 29.4 mM aqueous solution of $HAuCl_4$ (Alfa Aesar; #36 400) was performed by quickly adding 200 µL of $NaBH_4$ aqueous solution (211 mM; Sigma-Aldrich, #452 882) to the mixture under vigorous stirring. The so-formed gold ultrasmall nanoparticles (USNPs) turned the mixture orange, and it was stirred for further 10 min at room temperature. Afterwards, the arrays were formed by slowly dropping PL-IRDye, and gently shaking the mixture for 20 min. The arrays were collected by centrifuging for 3 min at 15 658 rcf, resuspended in 2 mL of Milli-Q water, and sonicated to homogenize the mixture. A modified Stöber reaction was employed to form the silica shell: 70 mL of absolute ethanol (Sigma-Aldrich, #24 105) was added of 40 µL of tetraethyl orthosilicate (TEOS, 98%; Sigma-Aldrich #131 903) and 2.4 mL of ammonium hydroxide (Sigma-Aldrich, #221 228), and finally of the array suspension. After gentle shaking for 3 h, NAs were isolated by centrifuging at 3220 rcf for 30 min. NAs were resuspended in ethanol and washed several times with ethanol and Milli-Q water to remove the unreacted precursors. Bigger NAs were discarded by short spin (14 s at 16 873 rcf). The collected supernatant was washed once again in ethanol and stored in 1 mL of ethanol at −20 °C in the dark.

Synthesis of IRDye-Modified Thermo-Nanoarchitectures (tNAs-IRDye): Au USNPs were prepared as previously reported. After the quick addition of $NaBH_4$, 200 µL of 4,4′-dimercaptostilbene (DMSB, 4.09 mM in dimethylformamide, Sigma-Aldrich; #701 696) was dropped. The reaction mixture turned darker, and it was stirred for another 10 min. The arrays were formed by slowly adding PL-IRDye, and gently shaking the mixture for 20 min. The formation of the silica shell and the purification of the obtained *t*NAs-IRDye were performed as previously described. *t*NAs-IRDye were stored in 1 mL of ethanol at −20 °C in the dark.

Characterization of NAs:

1) *Dynamic Light Scattering (DLS) and zeta-potential measurements*. The hydrodynamic diameter of NAs-IRDye and *t*NAs-IRDye was measured with DLS after resuspension in 1X PBS pH 7.4. NAs suspension was placed in 1 mL quartz cuvette at 25 °C in a Zetasizer nano-ZS90

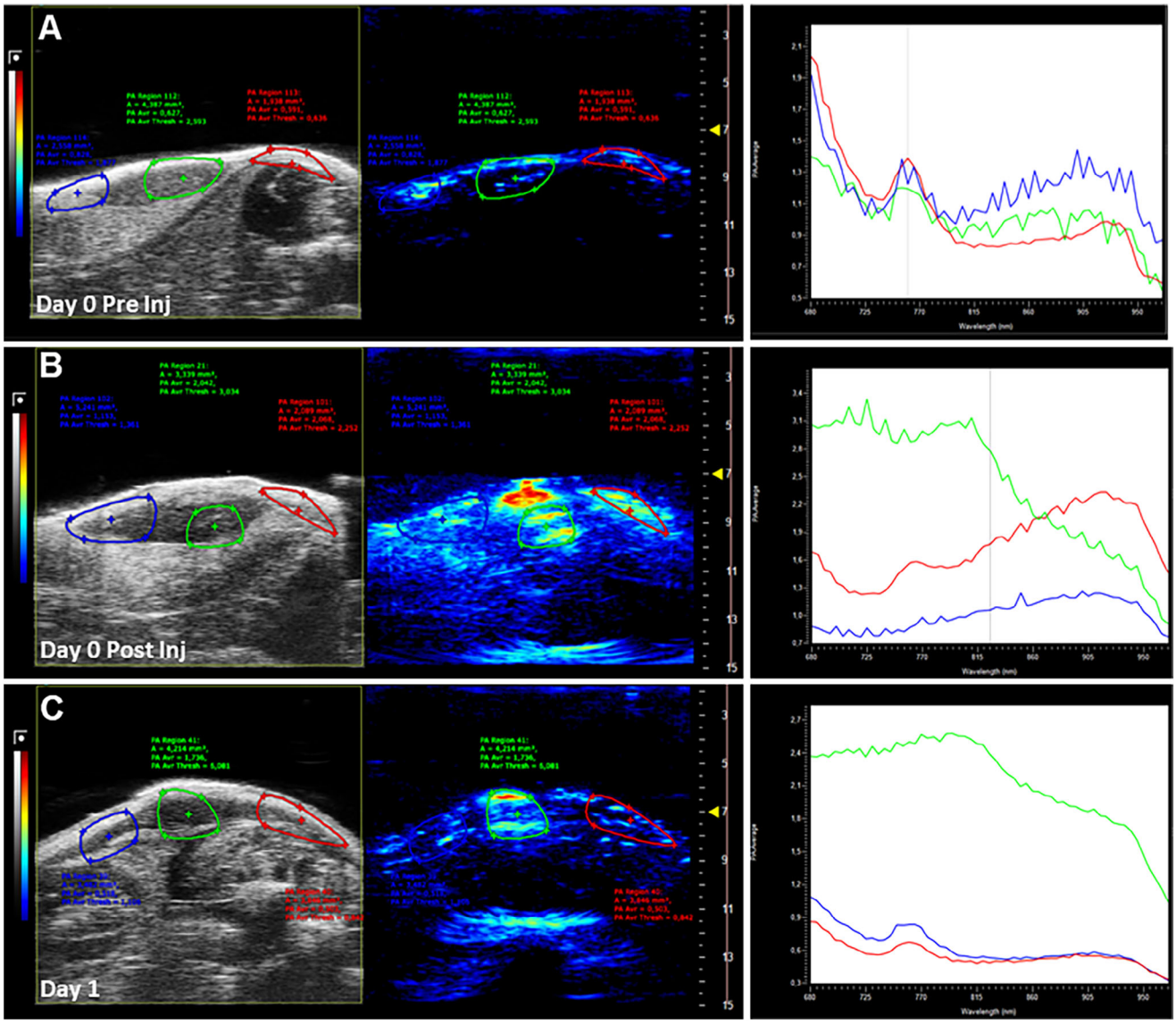

Figure 3. High-frequency – ultrasound (HF-US) images (grayscale) and PA images (rainbows scale) of a reference tumor on day 0 before A) and after B) *t*NAs-IRDye injection, and day 1 after PTT C). Each row reports the PA spectral trends calculated in three regions of interest (ROIs) inside the tumor injection site.

(Malvern Instruments, Malvern, United Kingdom) and analyzed with a single scattering angle of 90°. To measure the zeta-potential, NAs suspensions were transferred to DTS 1070 standard capillary cells.

2) *Transmission Electron Microscopy (TEM)*. The ethanol suspension of NAs was dropped on 300-mesh carbon-coated copper and dried before TEM acquisitions with ZEISS Libra 120, operated at 120 kV accelerating voltage.
3) *Inductively Coupled Plasma–Mass Spectrometry (ICP–MS) analysis*. The gold content in NAs-IRDye and *t*NAs-IRDye was assessed on an ICP–MS Agilent 7700 (Agilent Technologies, Santa Clara, CA, USA). To digest NAs samples, aqua regia was prepared by mixing 3:1 hydrochloric acid (34-37% in HCl, TraceMetal Grade; Thermo Fisher Scientific, #A508-P500) and nitric acid (65% Suprapur Sigma-Aldrich, #1.00441). Samples were subjected to 200 °C under a microwave irradiation protocol using CEM Discover SP-D digestion microwave (CEM, Matthews, NC, USA). The quantification with ICP-MS was performed by analysis against standard calibration curves (gold standard 1000 ppm; Absolute Standards, inc., #56 079) of the samples diluted with 3 mL of 3% nitric acid solution. 10 ppm Hg (10 000 ppm; Sigma-Aldrich, #75 111) in 3% nitric acid solution was used as the internal standard.
4) UV–vis *spectrophotometry*. 3 µg of Au in NAs-IRDye and *t*NAs-IRDye was centrifuged for 3 min at 16 873 rcf to remove ethanol and resuspended in 1X PBS pH 7.4. The samples were dropped on a Mettler Toledo UV5 Nano Spectrophotometer (Mettler Toledo, Columbus, OH, USA) with an optical path of 0.1035 cm. Lambert-Beer equation ($A = \epsilon lC$, where A = absorbance; ϵ = molar extinction coefficient (240 000 $M^{-1}cm^{-1}$); l = optical path (cm); C = concentration (M)) was used to estimate IRDye amount within NAs from the recorded absorbance at 774 nm. Spectra (already solvent-subtracted) were processed using Origin software (OriginLab Corporation) by smoothing the signal and then subtracting the contribution of particle scattering.

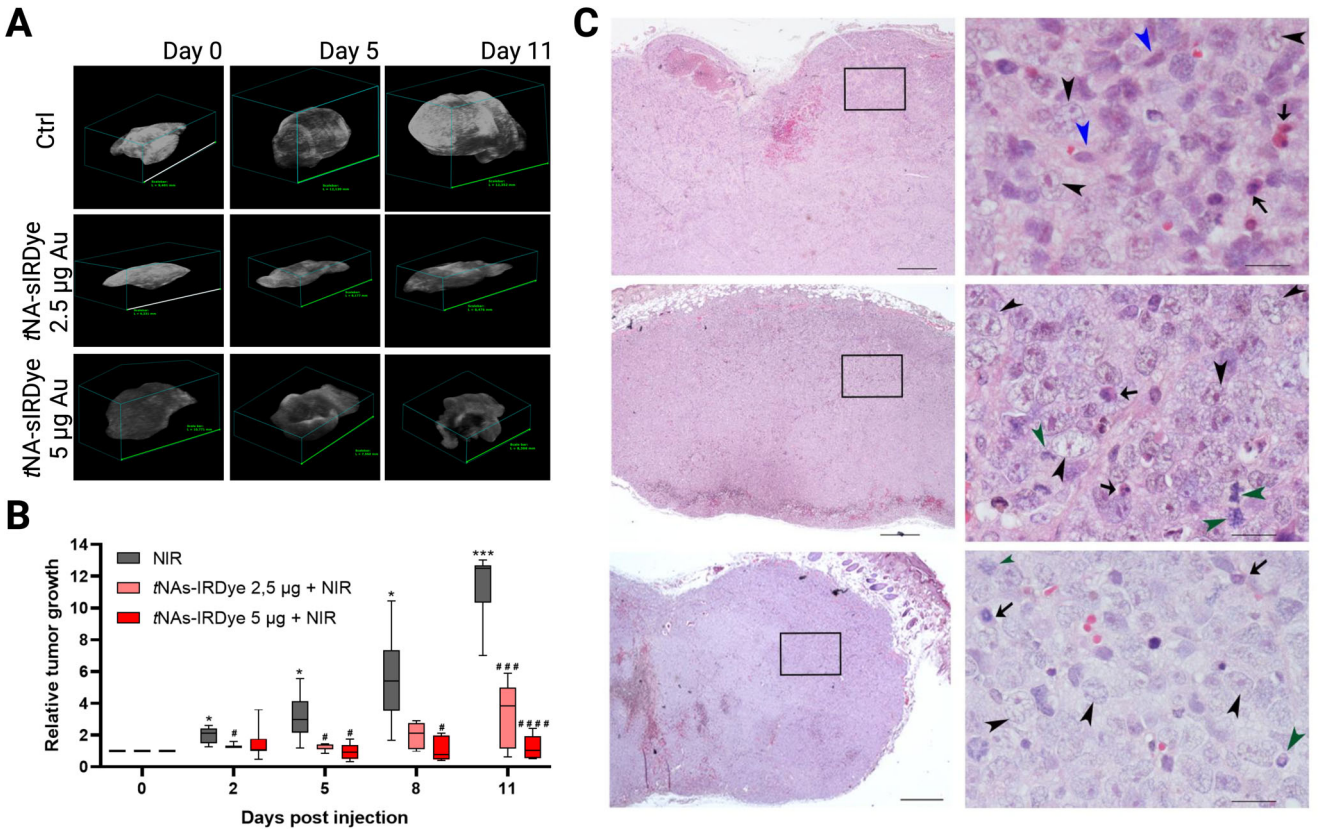

Figure 4. A) Representative 3D HF-US volume reconstruction of tumors treated with only NIR (Ctrl), 5 µg Au or 2.5 µg Au *t*NAs-IRDye + irradiation. The reconstructed volume refers to day 0, 5, and 11. B) Relative tumor growth after intratumoral injection of *t*NAs-IRDye 2.5 µg Au (salmon), *t*NAs-IRDye 5 µg of Au (red) or vehicle (gray) + PTT. Statistically significant values were indicated with asterisks or hashtags: $^{*}/^{\#}$—p <0.05, $^{**}/^{\#\#}$—p <0.01, $^{***}/^{\#\#\#}$—p <0.001, $^{****}/^{\#\#\#\#}$—p <0.0001. *D2, D5, D8, D11 versus D0 for each condition, # *t*NAs-IRDye versus vehicle (NIR). C) Hematoxylin eosin staining of tumors excised from the three experimental groups. Upper panels: NIR-treated tumor sample. Middle panels: tumor samples treated with *t*NAs-IRDye 2.5 µg + NIR irradiation. Lower panels: tumor samples treated with *t*NAs-IRDye 5 µg + NIR irradiation. Blue arrowheads: cells with normal appearance. Arrows: cells showing cytoplasmic acidophilia and chromatin condensation. Black arrowheads: cells showing vacuolization. Green arrowheads: cells showing karyolysis. Scale bar of left panels: 500 µm; scale bar of right panels: 20 µm.

Photoacoustic Characterization of NAs: The multispectral behavior and photostability of NAs under photoacoustic stimulation were studied in a validated custom-made test object (Figure S1, Supporting Information) and in ex vivo chicken breast samples.[35] For the test object experiments, NAs-IRDye, *t*NAs-IRDye (0.2 mg mL^{-1} in gold, PBS solution), and PBS (background signal) were loaded into polyethylene tubes and stimulated by pulsed laser illumination provided by the multimodal imaging platform Vevo 3100 and LAZR-X (Fujifilm VisualSonics INC.). The PA signals were acquired at 40 MHz central band using a Fujifilm Visualsonics MX-550 probe with 60 µm spatial resolution.

For the ex vivo experiments, chicken breast phantoms were injected with 50 µL of either NAs-IRDye or *t*NAs-IRDye (0.2 mg mL^{-1} in PBS) and handled as previously described for the test object experiments. In both conditions, the PA multispectral analysis was performed by stimulating the samples in the near-infrared optical range between 680 and 970 nm (NIR I) by 10 ns laser pulses with energies of the order of 50 mJ at 20 Hz pulse rate. The photostability assessment was checked under prolonged pulsed laser illumination at fixed wavelength at ≈800 nm for ≈30 s, corresponding to more than 500 laser shots.

In Vitro Photothermal Evaluations of NAs: The hyperthermic characterization of NAs was carried out by using a validated custom-made setup.[36] For the test, 500 µL of NAs-IRDye or *t*NAs-IRDye (50 µg mL^{-1} in gold, PBS solution) was loaded in a polystyrene cuvette and illuminated by a continuous wave (CW) laser diode at 808 nm (Thorlabs, Inc., US) for 15 min. The laser light was brought to the cuvette through a multimodal optical fiber (1 mm Ø, Thorlabs). The power of the laser light (400 mW) was monitored by a power meter sensor (Thorlabs). After the laser stimulation, the samples were allowed to cool for ≈10 min to reach room temperature. The change in temperature was monitored by a NIR camera (Heinamnn Sensors, Germany) placed in front of the cuvette. The hyperthermic trends were analyzed and fitted according to Wang's model[37]:

$$\Delta T\,(t) \;=\; a + be^{-x/\tau} \qquad (1)$$

where ΔT is the value of measured temperature respect the initial temperature of the illuminated sample, a represents the rate of absorption energy, while b the rate constant related to heat loss.

In Vivo Hyperthermic Tests: In vivo hyperthermic tests were conducted on healthy mice. The animals were placed on a sensorized table to monitor their physiological parameters: the heart and breath rate, and the body temperature. The laser was mounted on a mechanical leverage at a distance of ≈20 mm, perpendicular to the top of the tumor. A near-infrared camera was positioned in front of the tumor to acquire the thermal images (64 × 80 px, 10 Hz rate) and to assess the thermal gradient on the skin produced by laser irradiation (Figure S2, Supporting Information). To achieve an optimal laser illumination of the tumor, the laser power was set at 660 mW, leading to a mean power density of 0.67 W cm^{-2} in a selected spot size of 10 mm diameter. Laser power density was calculated in the same geometrical conditions of the in vivo experiment. Specifically, the 808 nm CW laser source was placed perpendicular to the power meter

(PM) sensor (S405C, Thorlabs) which was positioned on a controlled micrometric motorized linear stage (LHM-E, Zaber). Data of laser power distribution were acquired by moving the PM sensor in a range of 2 cm. The obtained data were elaborated and fit to calculate the mean values of the laser power distributed in a reference area (Matlab).

Cell Culture: Tongue squamous cell carcinoma HN-6 cells were cultured in DMEM supplemented with 10% heat-inactivated fetal bovine serum (FBS), 100 U mL^{-1} Penicillin, 100 mg mL^{-1} Streptomycin, and 2 mM L-glutamine (Sigma Aldrich) and maintained at 37 °C in a humified atmosphere of 5% CO_2 and 95% air.

In Vivo Photoacoustic Imaging and Photothermal Ablation: All the animal experiments were approved by the Ethical Committee of the Institute of Clinical Physiology and the Italian Ministry of Health (authorization n° 225/2020-PR). 12 female Foxn1^{nu} athymic nude mice (6–8 weeks, Envigo RMS srl, Milano, Italy) were implanted on both flanks with HN-6 cells (2^*10^6 cells in 100 µL of 1:1 Matrigel:PBS, per inoculation). After tumor induction, mice were monitored every day for their general conditions, weight, and tumor size (caliper method, $V_T = 0{,}5 \times L \times W^2$).

When the tumors reached a volume of ≈50 mm^3, mice were intratumorally injected with 10 µL of nano-architectures (2.5 or 5 µg of Au in sterile solution) or vehicle and then underwent photoacoustic-ultrasound (PAUS) imaging (day 0, D0) to confirm NAs localization and establish the precise initial tumor volume (US image segmentation). On day 1 (D1), both NAs- and vehicle-injected tumors were irradiated for 10 min with a NIR CW laser. The laser power was set at 660 mW, leading to a mean power density of 0.67 W cm^{-2} in a selected spot size of 10 mm diameter. Starting from day 2 (D2), tumors were evaluated through high frequency – ultrasound (HF-US, 40 MHz) imaging every three days up to day 11 (D11) for the evaluation of the volume of tumor growth. At the end of the experiment, tumors and organs were harvested and appropriately stored until further examination. PAUS images were processed by VevoLab software (FujiFilm Visualsonics, inc.), and the data were analyzed using Prism 10 (GraphPad Software).

Histological Analysis: After the treatments, the tumors were excised and fixed in 10% neutral buffered formalin. The samples (n = 3 for each experimental condition) were dehydrated and embedded in paraffin blocks. 5 µm-thick sections of the formalin-fixed, paraffin-embedded tissue blocks were cut with a microtome (Leica Microsystems, Milan, Italy) and attached to microscope slides by heating in an oven for 24 h at 37 °C. The paraffin sections were rehydrated in two baths of xylene followed by three baths of graded ethanol, stained with hematoxylin and eosin, and observed under a Nikon Eclipse E600 microscope (Nikon Instruments).

Quantification of Au in Tumors and Organs: Samples harvested from murine models (tumors and organs) were dried overnight at 80 °C to a constant weight. Samples were transferred in 10 mL-pressured vials and digested in aqua regia at 100 °C. When dried, samples were diluted with 2.5 mL of 3% nitric acid solution. Gold amount in tumors and organs was quantified via ICP-MS analysis against standard calibration curves as previously described.

Statistical Analysis: Data for the characterization of all NAs were presented as Mean ± SD. TEM images were analyzed with ImageJ software to determine the diameter of NAs and the thickness of their shell on at least 100 nanoparticles. Values of hydrodynamic diameter and zeta-potential were obtained by averaging at least three consecutive measurements.

Data in Figure S6 (Supporting Information) were analyzed by comparing the acquired datasets by using the analysis of variation tool (anova1), in the statistical toolbox of Matlab.

Data in Figure 4B were analyzed using Prism 10 (GraphPad Software) and presented as median (boxes) with whiskers indicating the minimum and maximum values (N = 8 for each condition). One-way ANOVA followed by post-hoc Tukey test was performed and p-values <0.05 were considered statistically significant.

Supporting Information

Supporting Information is available from the Wiley Online Library or from the author.

Acknowledgements

This work was supported by the MFAG 2017 – ID 19852 granted to V.V. from Associazione Italiana per la Ricerca sul Cancro (AIRC). The EuroBioImaging research infrastructure at the CNR Research Area provides open access to imaging technologies in biological and biomedical imaging, supporting this research. Figures were created with Biorender.com.

Conflict of Interest

The authors declare no conflicts of interest.

Author Contributions

P.A., M.L.E., L.M., and V.V. shared senior authorship. V.F. and C.C. contributed equally to this work. Synthesis and characterizations performed by V.F., M.L.E., A.Z., and G.D.; In vivo experiments performed by C.C., P.A., L.M., M.C., V.B.; Data analysis performed by C.C., P.A., L.M.; Funding validated by V.V.; Project design and coordination acquired by L.M., V.V. All Authors had discussed the data and contributed to writing the manuscript.

Data Availability Statement

The data that support the findings of this study are available from the corresponding author upon reasonable request.

Keywords

head/neck carcinoma, nanomaterials, photoacoustic imaging, photothermal treatment, theranostics

Received: March 11, 2024
Revised: May 13, 2024
Published online:

[1] D. E. Johnson, B. Burtness, C. R. Leemans, V. W. Y. Lui, J. E. Bauman, J. R. Grandis, *Nat. Rev. Dis. Prim.* **2020**, *6*, 92.
[2] J.-P. Machiels, C. René Leemans, W. Golusinski, C. Grau, L. Licitra, V. Gregoire, *Annals of Oncology* **2020**, *31*, 1462.
[3] S. F. Powell, L. Vu, W. C. Spanos, D. Pyeon, *Cancers (Basel)* **2021**, *13*, 5206.
[4] R. H. de Roest, M. van der Heijden, F. W. R. Wesseling, E. J. de Ruiter, M. W. Heymans, C. Terhaard, M. R. Vergeer, J. Buter, L. A. Devriese, J. P. de Boer, A. Navran, A. Hoeben, C. Vens, M. van den Brekel, R. H. Brakenhoff, C. R. Leemans, F. Hoebers, *Radiother. Oncol.* **2022**, *175*, 112.
[5] R. Saddawi-Konefka, S. Schokrpur, A. J. Lui, J. S. Gutkind, *Cancer J.* **2022**, *28*, 339.
[6] B. Goel, A. K. Tiwari, R. K. Pandey, A. P. Singh, S. Kumar, A. Sinha, S. K. Jain, A. Khattri, *Translational Oncology* **2022**, *21*, 101426.
[7] G. Xu, X. Bao, J. Chen, B. Zhang, D. Li, D. Zhou, X. Wang, C. Liu, Y. Wang, S. Qu, *Adv. Healthcare Mater.* **2019**, *8*, 1.
[8] P. Huang, P. Rong, J. Lin, W. Li, X. Yan, M. G. Zhang, L. Nie, G. Niu, J. Lu, W. Wang, X. Chen, *J. Am. Chem. Soc.* **2014**, *136*, 8307.
[9] J. F. Lovell, C. S. Jin, E. Huynh, H. Jin, C. Kim, J. L. Rubinstein, W. C. W. Chan, W. Cao, L. V. Wang, G. Zheng, *Nature Materials* **2011**, *10*, 324.
[10] Y. Liu, P. Bhattarai, Z. Dai, X. Chen, *Chem. Soc. Rev.* **2019**, *48*, 2053.
[11] P. K. Upputuri, M. Pramanik, *WIREs Nanomedicine and Nanobiotechnology* **2020**, https://doi.org/10.1002/wnan.1618.

[12] Y. Mantri, J. V. Jokerst, *ACS Nano* **2020**, *14*, 9408.
[13] J. Weber, P. C. Beard, S. E. Bohndiek, *Nat. Methods* **2016**, *13*, 639.
[14] A. Gonnelli, M. Gerbé de Thoré, M. L. Ermini, V. Frusca, A. Zamborlin, N. Signolle, O. Bawa, C. Clémenson, L. Meziani, P. Bergeron, I. El-Azrak, P. Sarogni, E. Mugnaioli, N. Giannini, G. Drava, E. Deutsch, F. Paiar, M. Mondini, V. Voliani, *Advanced Materials. Portico* **2024**, https://doi.org/10.1002/adma.202400949.
[15] C. Avigo, D. Cassano, C. Kusmic, V. Voliani, L. Menichetti, *J. Phys. Chem. C* **2017**, *121*, 6955.
[16] P. Armanetti, S. Pocoví-Martínez, A. Flori, C. Avigo, D. Cassano, L. Menichetti, V. Voliani, *Nanomed. Nanotechnol. Biol. Med.* **2018**, *14*, 1787.
[17] H. S. Han, K. Y. Choi, *Biomedicines* **2021**, *9*, 305.
[18] S. Yuan, J. Zhou, J. Wang, X. Ma, F. Liu, S. Chen, J.-X. Fan, G.-P. Yan, *Molecular Pharmaceutics* **2024**, *21*, 467.
[19] Q. Niu, Q. Sun, R. Bai, Y. Zhang, Z. Zhuang, X. Zhang, T. Xin, S. Chen, B. Han, *Int. J. Mol. Sci.* **2022**, *23*, 10428.
[20] G. González-Rubio, A. Guerrero-Martínez, L. M. Liz-Marzán, *Acc. Chem. Res.* **2016**, *49*, 678.
[21] D. Cassano, M. Santi, F. D'Autilia, A. K. Mapanao, S. Luin, V. Voliani, *Mater. Horiz.* **2019**, *6*, 531.
[22] A. K. Mapanao, P. Sarogni, M. Santi, M. Menicagli, A. Gonnelli, A. Zamborlin, M. L. Ermini, V. Voliani, *Biomater. Sci.* **2022**, *10*, 6135.
[23] D. Cassano, M. Summa, S. Pocoví-Martínez, A.-K. Mapanao, T. Catelani, R. Bertorelli, V. Voliani, *Part. Part. Syst. Charact.* **2019**, *36*, 1800464.
[24] A. K. Mapanao, G. Giannone, M. Summa, M. L. Ermini, A. Zamborlin, M. Santi, D. Cassano, R. Bertorelli, V. Voliani, *Nanoscale Adv.* **2020**, *2*, 3815.
[25] P. Sarogni, A. K. Mapanao, A. Gonnelli, M. L. Ermini, S. Marchetti, C. Kusmic, F. Paiar, V. Voliani, *iScience* **2022**, *25*, 103980.
[26] A. Zamborlin, P. Sarogni, V. Frusca, A. Gonnelli, N. Giannini, M. L. Ermini, A. Marranci, F. Pagliari, C. M. Mazzanti, J. Seco, V. Voliani, *ACS Appl. Nano Mater.* **2023**, *6*, 22532.
[27] M. Santi, A. K. Mapanao, D. Cassano, Y. Vlamidis, V. Cappello, V. Voliani, *Cancers* **2020**, *12*, 1063.
[28] A. Gonnelli, P. Sarogni, N. Giannini, S. Linsalata, F. Di Martino, A. Zamborlin, V. Frusca, M. L. Ermini, P. Puccini, V. Voliani, F. Paiar, *Artificial Cells, Nanomedicine, and Biotechnology* **2024**, *52*, 122.
[29] A. K. Mapanao, M. Santi, V. Voliani, *J. Colloid Interface Sci.* **2021**, *582*, 1003.
[30] L. Zhao, X. Zhang, X. Wang, X. Guan, W. Zhang, J. Ma, *J. Nanobiotechnol.* **2021**, *19*, 335.
[31] S. Bonvalot, C. Le Pechoux, T. De Baere, G. Kantor, X. Buy, E. Stoeckle, P. Terrier, P. Sargos, J. M. Coindre, N. Lassau, R. Ait Sarkouh, M. Dimitriu, E. Borghi, L. Levy, E. Deutsch, J.-C. Soria, *Clin. Cancer Res.* **2017**, *23*, 908.
[32] J. K. Cheong, E. H. Ooi, Y. S. Chiew, L. Menichetti, P. Armanetti, M. C. Franchini, E. Alchera, I. Locatelli, T. Canu, M. Maturi, V. Popov, M. Alfano, *Comput. Methods Programs Biomed.* **2023**, *230*, 107363.
[33] D. Villaret, B. Glisson, D. Kenady, E. Hanna, M. Carey, L. Gleich, G. H. Yoo, N. Futran, M. Hung, P. Anklesaria, A. E. Heald, *Head Neck* **2002**, *24*, 661.
[34] E. E. W. Cohen, L. Nabell, D. J. Wong, T. Day, G. A. Daniels, M. Milhem, S. Deva, M. Jameson, O. Guntinas-Lichius, M. Almubarak, M. Strother, E. Whitman, M. Chisamore, C. Obiozor, T. Bagulho, J. Gomez-Romo, C. Guiducci, R. Janssen, E. Gamelin, A. P. Algazi, *Clin. Cancer Res.* **2022**, *28*, 1157.
[35] P. Armanetti, A. Chillà, F. Margheri, A. Biagioni, L. Menichetti, G. Margheri, F. Ratto, S. Centi, F. Bianchini, M. Severi, R. Traversi, D. Bani, M. Lulli, T. Del Rosso, A. Mocali, E. Rovida, M. Del Rosso, G. Fibbi, A. Laurenzana, *Adv. Sci.* **2021**, *8*, 2001175.
[36] M. Alfano, E. Alchera, A. Sacchi, A. Gori, G. Quilici, I. Locatelli, C. Venegoni, R. Lucianò, A. M. Gasparri, B. Colombo, G. Taiè, J. Jose, P. Armanetti, L. Menichetti, G. Musco, A. Salonia, A. Corti, F. Curnis, *J. Nanobiotechnol.* **2023**, *21*, 301.
[37] X. Wang, G. Li, Y. Ding, S. Sun, *RSC Adv.* **2014**, *4*, 30375.